

Quasi-Vertical β -Ga₂O₃ Schottky Diodes on Sapphire Using All-LPCVD Growth and Plasma-Free Ga-Assisted Etching

Saleh Ahmed Khan¹, Ahmed Ibreljic¹, A F M Anhar Uddin Bhuiyan^{1, a)}

¹Department of Electrical and Computer Engineering, University of Massachusetts Lowell, MA 01854, USA

^{a)} Corresponding author Email: anhar_bhuiyan@uml.edu

Abstract

This work demonstrates quasi-vertical β -Ga₂O₃ Schottky barrier diodes (SBDs) fabricated on c-plane sapphire substrates using an all-low-pressure chemical vapor deposition (LPCVD)-based, plasma-free process flow that integrates both epitaxial growth of high-quality β -Ga₂O₃ heteroepitaxial film with an in-situ Ga-assisted β -Ga₂O₃ etching. A 6.3 μm thick ($\bar{2}01$) oriented β -Ga₂O₃ epitaxial layer structure was grown on c-plane sapphire with 6° miscut, comprising a moderately doped ($2.1 \times 10^{17} \text{ cm}^{-3}$) 3.15 μm thick drift layer and a heavily doped ($1 \times 10^{19} \text{ cm}^{-3}$) contact layer on an unintentionally doped buffer layer. Mesa isolation was achieved via Ga-assisted plasma-free LPCVD etching, producing vertically etched profiles with an etch depth of 3.6 μm . The fabricated SBDs exhibited excellent forward Current-Voltage (J-V) characteristics, including a turn-on voltage of 1.22 V, an ideality factor of 1.29, and a Schottky barrier height of 0.83 eV. The minimum differential specific on-resistance was measured to be $8.6 \text{ m}\Omega \cdot \text{cm}^2$, and the devices demonstrated high current density capability (252 A/cm^2 at 5 V). Capacitance-Voltage (C-V) analysis revealed a net carrier concentration of $2.1 \times 10^{17} \text{ cm}^{-3}$, uniformly distributed across the β -Ga₂O₃ drift layer. Temperature-dependent J-V-T measurements from 25 °C to 250 °C revealed thermionic emission-dominated transport with strong thermal stability. The Schottky barrier height increased from 0.80 eV to 1.16 eV, and the ideality factor rose modestly from 1.31 to 1.42 over this temperature range. Reverse leakage current remained low, increasing from $\sim 5 \times 10^{-6} \text{ A/cm}^2$ at 25 °C to $\sim 1 \times 10^{-4} \text{ A/cm}^2$ at 250 °C, with the $I_{\text{on}}/I_{\text{off}}$ ratio decreasing from $\sim 1 \times 10^7$ to 5×10^5 . The

devices achieved breakdown voltages ranging from 73 V to 100 V, corresponding to electric field strengths of 1.66 - 1.94 MV/cm. These results highlight the potential of LPCVD-grown and etched β -Ga₂O₃ devices for high-performance, thermally resilient power electronics applications.

Keywords: *Ultra-wide bandgap semiconductor, β -Ga₂O₃, low pressure chemical vapor deposition (LPCVD), in-situ, Ga-assisted LPCVD etching*

I. Introduction

β -Ga₂O₃ stands out as a promising ultra-wide bandgap semiconductor for next-generation high-voltage, high-efficiency power electronics, due to its ultrawide bandgap (~ 4.8 eV), high breakdown electric field (6-8 MV/cm), and the availability of low-cost, large-area native substrates grown by melt-based growth methods¹. These characteristics result in a Baliga's figure of merit that surpasses those of conventional wide bandgap power semiconductors such as SiC and GaN, making β -Ga₂O₃ an ideal candidate for next-generation power conversion systems, radio-frequency amplification, and extreme-environment electronics²⁻⁷. Substantial progress in high-quality β -Ga₂O₃ epitaxial film growth has enabled the realization of both lateral and vertical device architectures with excellent breakdown strength and thermal stability⁸⁻³⁵. To fully leverage the potential of β -Ga₂O₃ in high-power vertical device architectures, precise control over vertical isolation and trench formation is essential. This requires fabrication techniques capable of defining deep, high-aspect-ratio structures with minimal damage and high fidelity. However, the absence of p-type doping in β -Ga₂O₃ necessitates electric field control through mesa, trench, or fin geometries, structures that are highly sensitive to processing-induced surface degradation. Conventional plasma-based dry etching techniques can produce anisotropic profiles in β -Ga₂O₃ but often lead to lattice distortion and damage at the sidewalls of etched regions^{36, 37}, which can degrade overall device performance. To reduce such damage, alternative approaches including wet

chemical etching³⁸⁻⁴⁰, metal-assisted chemical etching (MacEtch)^{41,42}, and in-situ etching in MBE^{43, 44}, MOCVD⁴⁵, and HVPE⁴⁶⁻⁴⁸ systems have been explored. We recently developed an innovative Ga-assisted LPCVD based in-situ etching technique using solid-source metallic Ga as etchant, which enables anisotropic and plasma-free patterning of β -Ga₂O₃⁴⁹. This technique exploits a thermally activated surface reaction in an oxygen-deficient low-pressure CVD environment, leading to the formation of volatile Ga₂O suboxides that facilitate selective material removal. The etch chemistry: $4\text{Ga} + \text{Ga}_2\text{O}_3 \rightarrow 3\text{Ga}_2\text{O}$ proceeds cleanly under LPCVD conditions, avoiding the formation of plasma-induced surface states or subsurface defects. Through systematic studies, we demonstrated that the etch rate is tunable by controlling the Ga source-to-substrate distance, process temperature, and carrier gas flow rate, with peak etch rates exceeding $\sim 2.25 \mu\text{m/hr}$ under optimized conditions. In addition to achieving high etch rates, our LPCVD-based etching technique also exhibited a strong crystallographic selectivity and in-plane anisotropy. On (010)-oriented β -Ga₂O₃ substrates, trenches aligned along the (100) orientation yielded the most stable sidewalls, smooth, vertical, and with minimal lateral undercut, indicating that LPCVD based metallic Ga-assisted etching can achieve orientation-controlled 3D structures, essential for high power β -Ga₂O₃ vertical devices.

Building upon this foundational etching technology in LPCVD environment, this work demonstrates the LPCVD-grown ($\bar{2}01$) β -Ga₂O₃ quasi-vertical Schottky barrier diodes (SBDs) fabricated on insulating c-plane sapphire substrates, utilizing a fully plasma-free LPCVD growth and etching process. While β -Ga₂O₃ native substrates offer excellent lattice matching for developing high-quality epitaxial drift layer, their widespread adoption is still limited by high substrate cost and inherently low thermal conductivity. Sapphire, in contrast, combines excellent electrical isolation from its wide bandgap, mechanical robustness, relatively higher thermal

conductivity, and significantly lower cost, making it an attractive platform for scalable power devices. One potential drawback of using sapphire could be its lattice mismatch with β -Ga₂O₃. However, this challenge is also addressed by orienting β -Ga₂O₃ growth along its ($\bar{2}01$) orientation, which supports high-quality epitaxial film formation. Additionally, the use of offcut c-plane sapphire substrates (6° miscut) further promotes step-flow growth with smoother surface morphology. Our LPCVD technique has already demonstrated excellent film quality with high growth rates, as evidenced by our recent work where electron mobilities up to 149 cm²/V·s at carrier concentration of 1.15×10^{17} cm⁻³ were achieved in β -Ga₂O₃ films grown on off-axis sapphire substrates¹⁰. In this work, we integrate, for the first time, the high-quality LPCVD-grown β -Ga₂O₃ epitaxy with in-situ Ga-assisted LPCVD etching process to realize quasi-vertical Schottky barrier diodes on insulating c-plane sapphire substrates- all within a fully plasma-free process flow. This combined approach not only minimizes interface damage but also simplifies process integration and reduces fabrication overhead.

II. Experimental Details

II. A. LPCVD Growth of β -Ga₂O₃ Epitaxial Stack:

The ($\bar{2}01$) β -Ga₂O₃ epitaxial layers were grown in a custom-designed LPCVD chamber on c-plane sapphire substrates with a 6° miscut. This intentional off-axis orientation facilitates step-flow growth and suppresses defect formation, enabling high crystalline quality of the epitaxial film^{10, 28, 50}. Prior to growth, the substrate was sequentially cleaned with acetone, isopropyl alcohol (IPA), and deionized (DI) water, followed by nitrogen blow-drying. Ultra-high purity argon (99.9999%) was used as both the carrier and purge gas, while oxygen (99.999%) and metallic gallium pellets (99.99999%) served as the oxygen and gallium sources, respectively. Silicon tetrachloride (SiCl₄) was introduced as the n-type dopant, with flow rates adjusted to achieve desired doping

concentrations. The growth was carried out at a substrate temperature of 1000 °C and a chamber pressure of ~1.5 Torr, with the substrate placed 7 cm from the gallium source. The epitaxial stack consisted of three distinct layers with a total thickness of 6.3 μm. Growth began with a 10-minute unintentionally doped (UID) β-Ga₂O₃ buffer layer (1.05 μm thick) grown without any SiCl₄ flow. This was followed by a 20-minute growth of n⁺ Si-doped β-Ga₂O₃ layer (2.10 μm thick) using a SiCl₄ flow rate of 0.5 sccm to achieve a high doping concentration of 1×10¹⁹ cm⁻³, forming the contact layer for the Schottky barrier diode. Finally, the Si doped β-Ga₂O₃ drift layer was grown for 30 minutes using a reduced SiCl₄ flow rate of 0.001 sccm, targeting a doping concentration of 2.1 × 10¹⁷ cm⁻³ and achieving a total thickness of 3.15 μm.

II. B. Plasma-Damage Free Etching of β-Ga₂O₃ using LPCVD:

Plasma-free mesa isolation was achieved using our custom-built horizontal LPCVD system, where etching is driven by the thermal reaction between β-Ga₂O₃ and upstream metallic Ga vapor in an oxygen-deficient environment. The etch process was conducted at 1050 °C and a pressure of ~1.2 Torr, with the sample placed 2 cm downstream from the solid Ga source. Ultra-high purity argon (99.9999%) was used as the carrier and purge gas. Prior to etching, the samples were cleaned using acetone, IPA, and DI water, followed by nitrogen blow-drying. A 100 nm-thick SiO₂ hard mask was deposited using plasma-enhanced chemical vapor deposition (PECVD) and patterned via optical lithography to expose the regions targeted for etching. The samples were etched for 2 hours and 15 minutes, resulting in a measured etch depth of 3.6 μm, corresponding to an average etch rate of 1.6 μm/hr. This etch depth was intentionally selected to fully remove the drift layer and selectively reach into the n⁺ region, enabling device isolation and providing access to the n⁺ layer for subsequent ohmic contact formation. After etching, the SiO₂ mask was removed using a 1:50 diluted buffered oxide etch (BOE).

II. C. Structural, Surface Morphological, and Chemical Characterization

The surface morphology of the β -Ga₂O₃ epi-stack was characterized using a JEOL JSM-7401F field-emission scanning electron microscope (FESEM) to visualize surface texture and etch profiles, and a Park Systems XE-100 atomic force microscope (AFM) operated in tapping mode to quantify nanoscale roughness. The crystalline structure, phase purity, and orientation of the films were evaluated by high-resolution X-ray diffraction (XRD) using a Rigaku SmartLab diffractometer equipped with a Cu K α radiation source ($\lambda = 1.5418 \text{ \AA}$). Wide-angle 2θ - ω scans and rocking curves (ω -scans) were used to confirm phase purity and determine the out-of-plane crystalline orientation. Raman spectroscopy was carried out using a Horiba LabRam Evolution Raman spectrometer with a 532 nm excitation source to assess phonon modes and verify structural integrity before and after etching. X-ray photoelectron spectroscopy (XPS) measurements were performed using a Thermo Scientific XPS system with a monochromated Al K α X-ray source ($E = 1486.6 \text{ eV}$) to analyze chemical composition and bonding states. High-resolution scans of the Ga 3s and O 1s core levels were used to calculate the O/Ga ratio and monitor potential changes in surface chemistry following the LPCVD-based etching process.

II. D. Quasi-Vertical β -Ga₂O₃ Schottky Diode Fabrication

Following mesa isolation by LPCVD Ga-assisted etching, device fabrication was completed using sequential photolithography, passivation, metallization, and annealing steps. First, a 200 nm-thick SiO₂ passivation layer was deposited across the entire wafer surface using PECVD. Photolithography and buffered oxide etch (BOE) were then used to open windows in the SiO₂ layer to define the cathode region. A Ti/Au (20 nm/50 nm) metal stack was deposited by electron-beam evaporation and patterned via lift-off to form the cathode contact on the β -Ga₂O₃ surface surrounding the recessed mesa. This was followed by rapid thermal annealing (RTA) at 470 °C for

1 min in nitrogen ambient to improve metal-semiconductor contact characteristics. Subsequently, a second photolithography step was used to define the anode contact region. Ni/Au (30 nm/50 nm) was deposited via electron-beam evaporation and patterned using lift-off to form the Schottky contact on top of the etched mesa. The final device structure and full fabrication process flow are illustrated in Figs. 1(a) and (d), with the FESEM and AFM images (Figs. 1(b) and (c)) confirming an etch depth of 3.6 μm . Post-fabrication electrical characterization, including room-temperature and high-temperature (up to 250 $^{\circ}\text{C}$) Current-Voltage (J-V), Capacitance-Voltage (C-V) and reverse breakdown measurements, was performed using a Keithley 4200A-SCS Semiconductor Parameter Analyzer.

III. Results and Discussions

To evaluate the material quality of the heteroepitaxial $\beta\text{-Ga}_2\text{O}_3$ epitaxial stack used for device fabrication, comprehensive structural and morphological characterization was performed. Figure 2(a) shows a top-view FESEM image that reveals distinct step-flow surface morphology, indicative of epitaxial layer-by-layer growth. The surface AFM scan in Fig. 2(b) shows uniform morphology with step-flow features and an RMS roughness of 4.7 nm, confirming a smooth and well-ordered surface. These morphological features are characteristic of step-flow growth on off-axis sapphire substrates, consistent with our prior work on LPCVD-grown high quality ($\bar{2}01$) $\beta\text{-Ga}_2\text{O}_3$ films with similar doping levels ¹⁰.

High-resolution X-ray diffraction (XRD) analysis further confirmed the film's structural quality and phase purity. As shown in Fig. 2(c), strong diffraction peaks corresponding exclusively to the ($\bar{h}0l$) family of monoclinic $\beta\text{-Ga}_2\text{O}_3$ planes are observed, with no evidence of secondary phases. The presence of higher-order ($\bar{2}01$) peaks such as ($\bar{4}02$), ($\bar{6}03$), and ($\bar{8}04$) signifies coherent long-range ordering and crystallographic orientation fidelity. The rocking curve (ω -scan)

of the ($\bar{4}02$) reflection, shown in Fig. 2(d), exhibits a narrow full width at half maximum (FWHM) of 287 arcsec. This value is among the lowest reported for heteroepitaxial β -Ga₂O₃ film on sapphire, typically achieved using epitaxial techniques such as MOCVD and MBE⁵⁰⁻⁵⁴.

To evaluate the structural integrity of the heteroepitaxial β -Ga₂O₃ film before and after Ga-assisted in-situ LPCVD etching, Raman spectroscopy was performed on both the pristine (unetched) and etched surfaces, as shown in Fig. 3. The Raman spectra exhibit characteristic vibrational modes corresponding to monoclinic ($\bar{2}01$) β -Ga₂O₃, with distinct peaks attributed to both A_g and B_g phonon symmetries. These modes arise from the 30 phonon modes predicted by group theory for monoclinic β -Ga₂O₃, of which 27 are optical and 3 are acoustic. The optical modes are classified as 10 A_g, 5 B_g, 4 A_u, and 8 B_u, where the A_g and B_g modes are Raman-active, and the A_u and B_u modes are infrared-active⁵⁵. In the spectra of the heteroepitaxial ($\bar{2}01$) β -Ga₂O₃ films, distinct peaks are observed at 114.1, 144.3, 474.1, and 652.5 cm⁻¹, corresponding to B_g modes, and at 169.3, 200.1, 319.3, 347.1, 416.2, 630.5, and 766.7 cm⁻¹, corresponding to A_g modes. These peak positions are in good agreement with previous experimental and theoretical studies^{50, 55}. Importantly, the Raman signatures from the etched surface show no shift in peak position, no broadening, and no suppression of the fundamental vibrational modes compared to the pristine surface. This indicates that the LPCVD-based Ga-assisted etching process preserves the lattice symmetry and does not introduce structural degradation, rotational domains or phase transformation. The intensity of sapphire-related modes remains similar between the two spectra, further confirming that the optical penetration depth remains consistent and the observed phonon modes are intrinsic to the β -Ga₂O₃ layer. The retention of both A_g and B_g modes with sharp and symmetric profiles indicates good crystalline quality of both pristine and etched film surface.

To investigate the surface chemistry before and after etching, X-ray photoelectron spectroscopy (XPS) was performed on both the pristine and etched β -Ga₂O₃ surfaces, as shown in Fig. 4. The wide-range survey spectra reveal distinct peaks corresponding to Ga and O, with no detectable metallic contamination, confirming the chemical purity of both surfaces. Notably, no silicon-related peaks were detected on the etched surface within the sensitivity limits of XPS, suggesting that any potential Si diffusion from the SiO₂ mask into the β -Ga₂O₃ surface might not occur under etching process conditions. High-resolution scans of the Ga 3s and O 1s regions were used for quantitative analysis. High-resolution O 1s spectra were deconvoluted into two components: a primary peak centered near 530.9 eV corresponding to lattice oxygen (Ga–O), and a secondary peak near 532.3 eV attributed to surface hydroxyl groups (O–H). The Ga 3s peak remained sharp and symmetric, indicating stable Ga–O bonding. Using sensitivity-factor-corrected areas of the O 1s and Ga 3s peaks, the O/Ga atomic ratio was calculated to be 1.49 (Oxygen: 59.81%, Gallium: 40.19%) for the unetched surface and 1.45 (Oxygen: 59.25%, Gallium: 40.75%) for the etched surface. These results indicate that both the pristine and etched surfaces retain their chemical integrity and near-stoichiometric composition.

Following the comprehensive structural, morphological, and chemical characterization of the LPCVD-grown β -Ga₂O₃ epitaxial stack, the electrical performance of the fabricated Schottky barrier diodes was evaluated to further assess the impact of the LPCVD-grown and etched β -Ga₂O₃ layers on device behavior. The current-voltage (J-V) characteristics of the diode, shown in Fig. 5(a), demonstrate excellent rectifying behavior with a clear exponential increase in forward current and a low leakage current in reverse bias. The device exhibits a low turn-on voltage ($V_{\text{turn-on}}$) of 1.22 V (assuming an on-state current density of 1 A cm⁻²) and an ideality factor (η) of 1.29, indicating near-ideal thermionic emission transport across the metal-semiconductor junction. The

extracted Schottky barrier height (Φ_B) of 0.83 eV is consistent with typical Ni/ β -Ga₂O₃ contacts and reflects good interface quality. The minimum differential specific on-resistance ($R_{on,sp}$) was determined to be 8.6 m Ω ·cm². This low $R_{on,sp}$ value confirms efficient current transport through the epitaxial stack and effective contact formation on the recessed n⁺ β -Ga₂O₃ layer. The high current density capability of 252 A/cm² at 5 V further highlights the advantages of plasma-free etching and the excellent material quality achieved through LPCVD-grown β -Ga₂O₃. It is important to note that etch-induced damage, particularly along the mesa sidewalls in close proximity to the active junction edge, can significantly degrade diode performance, affecting leakage current, ideality factor, and on-resistance. Conventional plasma-based reactive ion etching (RIE) techniques have been reported to introduce structural and chemical damage in β -Ga₂O₃, often necessitating additional post-etch treatments to restore interface quality^{56, 57}. In contrast, the Ga-assisted in-situ LPCVD etching approach employed in this work offers a damage-free, thermally driven alternative that avoids ion bombardment and is expected to preserve the integrity of the etched sidewalls, as reflected in the low ideality factor and good rectification behavior observed in our devices.

To further evaluate the doping and junction properties, C-V measurements were performed, as shown in Fig. 5(b). The capacitance decreased with increasing reverse bias, and the corresponding 1/C²-V plot exhibited a linear relationship, characteristic of a uniformly doped Schottky junction. The V_{bi} and $N_d^+ - N_a^-$ are determined using the following formulas using the relative permittivity of β -Ga₂O₃, $\epsilon_r = 10$, density of states in the conduction band, $N_C = 5.2 \times 10^{18}$ cm⁻³, where A representing the device area^{58, 59}.

$$N_d^+ - N_a^- = \frac{2}{q\epsilon_r\epsilon_0 A^2 \left(\frac{d\frac{1}{C^2}}{dV} \right)} \quad (1)$$

$$\frac{A^2}{C^2} = qV_{bi} + \frac{kT}{q} \ln\left[\frac{N_c}{N_d^+ - N_a^-}\right] \quad (2)$$

The built-in potential (V_{bi}), estimated by extrapolating the linear region of the $1/C^2$ - V curve to the voltage axis, was found to be ~ 3.67 V. From the C-V analysis, an average net carrier density ($N_d^+ - N_a^-$) of $2.1 \times 10^{17} \text{ cm}^{-3}$ was extracted, matching well with the doping level targeted for the ($\bar{2}01$) β -Ga₂O₃ drift layer. As shown in Figure 5(c), the net carrier density profile is flat and uniform across the drift layer, confirming the consistency of doping achieved during the epitaxial growth process. Additionally, no clear indication of an upward slope or surface donor accumulation is observed in the carrier density profile, suggesting that the high-temperature in-situ LPCVD etching process did not lead to any noticeable dopant diffusion from the SiO₂ mask, consistent with prior studies reporting minimal interdiffusion at β -Ga₂O₃/SiO₂ interfaces even after annealing at high temperatures⁶⁰.

To assess the thermal stability and transport mechanisms of the β -Ga₂O₃ Schottky barrier diodes fabricated on sapphire substrates, temperature-dependent current-voltage (J-V-T) measurements were performed from 25 °C to 250 °C, as shown in Fig. 6. In the linear-scale forward J-V plots shown in Fig. 6(a), the forward current density increases with temperature, which is characteristic of thermionic emission over the Schottky barrier. As the temperature rises, electrons gain additional thermal energy, increasing their probability of surmounting the Schottky barrier and resulting in enhanced forward conduction. This temperature-enhanced barrier injection becomes particularly prominent at low-to-moderate forward bias, where transport is barrier-limited and governed by the Schottky diode equations:

$$J = J_s \left[\exp\left(\frac{qV}{\eta k_0 T}\right) - 1 \right] \quad (3)$$

$$J_s = A^* T^2 \exp\left(-\frac{q\Phi_B}{k_0 T}\right) \quad (4)$$

$$A^* = \frac{4\pi q m_n^* k_0^2}{h^3} \quad (5)$$

where q is the electric charge, k_0 is the Boltzmann constant, and η is the ideality factor, J_s is the reverse saturation current density, Φ_B is the Schottky barrier height, and A^* is Richardson's constant, which is calculated to be $41.04 \text{ A cm}^{-2} \text{ K}^{-2}$ ^{59, 61, 62}. The semi-logarithmic forward J–V characteristics (Fig. 6b) further illustrate this trend, revealing an increase in on-current from 53 to 90 A cm^{-2} from 25°C to 250°C at the same forward bias of 4V. Notably, while the current continues to rise with temperature in the barrier-limited regime (low bias), the increase saturates in the high bias (ohmic) region. This saturation is likely due to increased phonon scattering and reduced carrier mobility within the drift region and contact layers at elevated temperatures, a behavior typical in semiconductors where the electron-phonon interaction dominates at high fields and temperatures ⁶³. Additionally, self-heating and series resistance effects may begin to influence the I-V shape at high current levels ⁶¹, particularly in devices with small footprint and limited thermal sinking. Figure 6(c) quantifies the temperature dependence of $R_{\text{on,sp}}$ extracted from the linear region of the forward J-V characteristics. A non-monotonic trend is observed: while $R_{\text{on,sp}}$ initially decreases with increasing temperature in the low-to-moderate forward bias regime due to thermally assisted carrier injection, the inset reveals that $R_{\text{on,sp}}$ increases in the high-bias regime at elevated temperatures. This divergent behavior arises from two competing effects. At low biases, thermionic emission dominates and benefits from enhanced carrier activation and interface injection, which reduces the effective series resistance. However, at higher forward biases where the current becomes limited by the series resistance of the drift region, the dominant factor becomes carrier mobility. As the temperature increases, enhanced lattice vibrations increase electron–phonon scattering, leading to reduced electron mobility in the $\beta\text{-Ga}_2\text{O}_3$ drift region and thus a rise in $R_{\text{on,sp}}$ under high-field conditions. This trend, decreasing $R_{\text{on,sp}}$ at low bias and

increasing $R_{on,sp}$ at high bias with temperature, is characteristic of β -Ga₂O₃ Schottky barrier diodes and is consistent with earlier observations in radiation and thermally stressed devices^{24, 59, 64}. The ability to maintain rectifying behavior and consistent conduction characteristics over a wide temperature range, demonstrates the structural and electrical robustness of the LPCVD-grown β -Ga₂O₃ layers and the reliability of the plasma-free device processing strategy.

Figure 7 summarizes the extracted Schottky barrier height (Φ_B), ideality factor (η), reverse leakage current ($I_{reverse}$), and rectification ratio (I_{on}/I_{off}) as functions of temperature for the fabricated diodes. As shown in Fig. 7(a), the barrier height increases from 0.80 eV at 25 °C to 1.16 eV at 250 °C, consistent with the expectations of the thermionic emission (TE) model in the presence of barrier inhomogeneities⁶⁵⁻⁶⁹. At lower temperatures, current conduction tends to be dominated by electrons traversing lower-barrier patches at the metal/semiconductor interface. As temperature increases, more carriers acquire sufficient thermal energy to surmount higher barrier regions, effectively raising the extracted Φ_B . This phenomenon, attributed to lateral inhomogeneities in the Schottky contact, has been reported in previous literatures for ultra-wide bandgap semiconductors^{59, 70, 71}, and is typically associated with non-idealities, including interfacial disorder, grain boundaries, or residual contaminants. The extracted ideality factor η , also shown in Fig. 7(a), increases modestly from 1.31 at 25 °C to 1.42 at 250 °C. This slight increase with temperature suggests a gradual deviation from ideal thermionic emission behavior, potentially due to enhanced recombination or tunneling contributions at higher temperatures. In practice, temperature-induced changes in η can also reflect evolving interface conditions, including thermally activated trap-assisted transport or bias-dependent modulation of interface states. Nevertheless, the relatively low η across the full temperature range indicates a high-quality Schottky junction with minimal leakage paths and well-behaved transport characteristics. Figure

7(b) further evaluates the thermal stability of the diode by plotting the reverse leakage current (measured at -4 V) and the I_{on}/I_{off} ratio (measured at ± 4 V) as functions of temperature. As expected, reverse leakage current increases with temperature, rising from 4.9×10^{-6} A/cm² at 25 °C to 1.7×10^{-4} A/cm² at 250 °C. This behavior is typical of Schottky diodes and is attributed to thermally excited electrons gaining sufficient energy to surmount the barrier or engage in thermionic field emission processes^{59, 61, 65, 72}. The increase in leakage is particularly pronounced beyond 200 °C, where lattice vibrations and interfacial trap activity likely contribute to additional leakage channels. Consequently, the I_{on}/I_{off} ratio decreases with increasing temperature, dropping by nearly two orders of magnitude from 1×10^7 at 25 °C to below 5.3×10^5 at 250 °C. Despite this decline, the device maintains strong rectification performance across the full temperature range, which indicates the thermal resilience of the LPCVD-grown β -Ga₂O₃ stack and the plasma-free etch-defined mesa architecture. These results confirm that the device remains functional and rectifying at elevated temperatures, and the interface quality is preserved even in thermally stressed regimes.

Finally, to assess the reverse blocking capability of the fabricated β -Ga₂O₃ Schottky diodes, reverse breakdown measurements were performed under steady-state voltage sweep conditions, as shown in Fig. 8(a). The diodes exhibited breakdown voltages ranging from 73 V to 100 V, corresponding to parallel-plate electric field strengths between 1.66 MV/cm and 1.94 MV/cm. The parallel-plate field at the reverse breakdown condition was estimated using one-dimensional electrostatics, $E_{field} = \sqrt{\frac{qN_dV_{BR}}{\epsilon}}$, where q is the charge of the electron, N_d is the doping of the semiconductor, V_{BR} is the breakdown voltage, and ϵ is the permittivity of Ga₂O₃. It should be noted that the observed breakdown voltages are primarily influenced by the relatively high doping concentration (2.1×10^{17} cm⁻³) in the drift layer, which limits the depletion width and hence the

maximum sustainable field. Although the LPCVD-grown β -Ga₂O₃ layers exhibit good structural and morphological quality, substrate and interface-related effects cannot be entirely ruled out. The use of c-plane sapphire, while advantageous for its cost-effectiveness and electrical insulation, introduces lattice mismatch with β -Ga₂O₃. This mismatch may lead to interfacial strain and dislocations that, although not obvious in surface morphology or crystallinity measurements, can influence local electric field distribution under reverse bias. Furthermore, the heteroepitaxial interface and mesa geometry may also result in localized field crowding and early onset of breakdown.

To further investigate the reverse breakdown behavior and electric field distribution, two-dimensional Technology Computer-Aided Design (TCAD) simulations were conducted based on the device geometry. As shown in Fig. 8(b), the simulated reverse bias field profile at 100 V reveals a pronounced electric field concentration at the perimeter of the anode contact. This effect is further confirmed by the extracted 1D electric field profile along the AA' cutline in Fig. 8(c), which shows the peak electric field localized near the anode edge. These results align with common field crowding phenomena observed in vertical Schottky structures and emphasize the importance of careful peripheral contact layout and junction termination. Further improvements in field uniformity and breakdown performance could be achieved by incorporating optimized edge termination by deep etching or advanced field management designs in future device generations. Nevertheless, the results validate the feasibility of achieving consistent reverse blocking performance in quasi-vertical β -Ga₂O₃ Schottky diodes fabricated entirely through LPCVD growth and in-situ plasma-free etching. This integration pathway offers a scalable, plasma-damage-minimized approach for developing future high-voltage β -Ga₂O₃ devices, particularly when paired

with lower doping, thicker drift layers, engineered buffer architectures, and field management techniques.

IV. Conclusions

In summary, this work demonstrates the first realization of quasi-vertical β -Ga₂O₃ Schottky barrier diodes (SBDs) fabricated entirely using a plasma-free LPCVD-based process, from epitaxial growth to in-situ etching for mesa isolation, on insulating sapphire substrates. Leveraging a novel in-situ Ga-assisted LPCVD etching technique, we achieved anisotropic, damage-free mesa isolation with etch depths of 3.6 μm . The resulting SBDs showed excellent forward characteristics with an ideality factor of 1.29, a Schottky barrier height of 0.83 eV, and a low specific on-resistance of 8.6 $\text{m}\Omega\cdot\text{cm}^2$. Temperature-dependent I-V analysis revealed thermionic emission-dominated transport with strong thermal stability and a modest increase in Schottky barrier height and ideality factor, likely attributed to interface inhomogeneities and barrier non-uniformity. Devices exhibited low and stable reverse leakage characteristics and achieved breakdown fields up to 1.94 MV/cm. Although the breakdown voltage was limited by the relatively high drift layer doping concentration, the demonstrated reverse blocking capability, along with robust forward conduction and thermal performance, highlight the promise of LPCVD-grown and etched β -Ga₂O₃ devices. The integration of epitaxy and etching within a single LPCVD platform offers a scalable and low-damage fabrication route for next-generation UWBG power electronics. These results also provide a critical step toward enabling cost-effective, high-voltage, and thermally resilient β -Ga₂O₃-based device architectures on foreign substrates.

Data Availability

The data that support the findings of this study are available from the corresponding author upon reasonable request.

Conflict of Interest

The authors have no conflicts to disclose.

Acknowledgement

The authors acknowledge the funding support from the National Science Foundation (NSF) under award numbers 2501623 and 2532898.

References

1. A. J. Green, J. Speck, G. Xing, P. Moens, F. Allerstam, K. Gumaelius, T. Neyer, A. Arias-Purdue, V. Mehrotra and A. Kuramata et. al, APL Materials 10 (2), 029201 (2022).
2. M. Higashiwaki, K. Sasaki, A. Kuramata, T. Masui and S. Yamakoshi, Applied Physics Letters 100 (1), 013504 (2012).
3. M. Higashiwaki and G. H. Jessen, Appl. Phys. Lett. 112, 060401 (2018).
4. J. Liu, J. Lu and A. Bhuiyan, Materials Science in Semiconductor Processing 195, 109627 (2025).
5. A. Kuramata, K. Koshi, S. Watanabe, Y. Yamaoka, T. Masui and S. Yamakoshi, Japanese Journal of Applied Physics 55 (12), 1202A1202 (2016).
6. S. J. Pearton, J. Yang, P. H. Cary, F. Ren, J. Kim, M. J. Tadjer and M. A. Mastro, Applied Physics Reviews 5 (1), 011301 (2018).
7. P. Dong, J. Zhang, Q. Yan, Z. Liu, P. Ma, H. Zhou and Y. Hao, IEEE Electron Device Letters 43 (5), 765-768 (2022).
8. Z. Feng, A. Bhuiyan, M. R. Karim and H. Zhao, Applied Physics Letters 114 (25), 250601 (2019).
9. C. Peterson, A. Bhattacharyya, K. Chanchaiworawit, R. Kahler, S. Roy, Y. Liu, S. Rebollo, A. Kallistova, T. E. Mates and S. Krishnamoorthy, Applied Physics Letters 125 (18) (2024).
10. S. A. Khan, A. Ibreljic, S. Margiotto and A. Bhuiyan, Applied Physics Letters 126 (1) (2025).
11. A. Bhuiyan, Z. Feng, J. M. Johnson, Z. Chen, H.-L. Huang, J. Hwang and H. Zhao, Applied Physics Letters 115 (12), 120602 (2019).
12. A. Bhuiyan, Z. Feng, J. M. Johnson, H.-L. Huang, J. Sarker, M. Zhu, M. R. Karim, B. Mazumder, J. Hwang and H. Zhao, APL Materials 8 (3), 031104 (2020).
13. A. Bhuiyan, Z. Feng, J. M. Johnson, H.-L. Huang, J. Hwang and H. Zhao, Applied Physics Letters 117 (14), 142107 (2020).
14. Z. Feng, A. Bhuiyan, N. K. Kalarickal, S. Rajan and H. Zhao, Applied Physics Letters 117 (22), 222106 (2020).
15. A. Bhuiyan, Z. Feng, J. M. Johnson, H.-L. Huang, J. Hwang and H. Zhao, Crystal Growth & Design 20 (10), 6722-6730 (2020).

16. Z. Feng, A. Bhuiyan, Z. Xia, W. Moore, Z. Chen, J. F. McGlone, D. R. Daughton, A. R. Arehart, S. A. Ringel, S. Rajan and H. Zhao, *physica status solidi (RRL) – Rapid Research Letters* 14 (8), 2000145 (2020).
17. A. Bhuiyan, Z. Feng, H.-L. Huang, L. Meng, J. Hwang and H. Zhao, *Journal of Vacuum Science & Technology A* 39 (6), 063207 (2021).
18. A. Bhuiyan, Z. Feng, L. Meng and H. Zhao, *Journal of Materials Research* 36 (23), 4804-4815 (2021).
19. N. K. Kalarickal, Z. Feng, A. Bhuiyan, Z. Xia, W. Moore, J. F. McGlone, A. R. Arehart, S. A. Ringel, H. Zhao and S. Rajan, *IEEE Transactions on Electron Devices* 68 (1), 29-35 (2021).
20. A. Bhuiyan, Z. Feng, L. Meng, A. Fiedler, H.-L. Huang, A. T. Neal, E. Steinbrunner, S. Mou, J. Hwang, S. Rajan and H. Zhao, *J. Appl. Phys.* 131, 145301 (2022).
21. M. Lingyu, Z. Feng, A. Bhuiyan, and H. Zhao, *Crystal Growth & Design* 22(6), 3896 (2022).
22. A. Bhuiyan, Z. Feng, H.-L. Huang, L. Meng, J. Hwang and H. Zhao, *J. Vac. Sci. Technol. A* 40, 062704 (2022).
23. A. Bhuiyan, Z. Feng, L. Meng and H. Zhao, *J. Appl. Phys.* 133, 211103 (2023).
24. S. Khan, S. Saha, U. Singiseti and A. Bhuiyan, *Journal of Applied Physics* 136 (22) (2024).
25. J. Zhang, P. Dong, K. Dang, Y. Zhang, Q. Yan, H. Xiang, J. Su, Z. Liu, M. Si and J. Gao, *Nature communications* 13 (1), 3900 (2022).
26. A. Mauze, Y. Zhang, T. Itoh, F. Wu and J. S. Speck, *APL Materials* 8 (2), 021104 (2020).
27. Z. Wen, K. Khan, X. Zhai and E. Ahmadi, *Appl. Phys. Lett.* 122, 082101 (2023).
28. Y. Zhang, Z. Feng, M. R. Karim and H. Zhao, *Journal of Vacuum Science & Technology A* 38 (5), 050806 (2020).
29. H. N. Masten, J. S. Lundh, T. I. Feygelson, K. Sasaki, Z. Cheng, J. A. Spencer, P.-Y. Liao, J. K. Hite, D. J. Pennachio, A. G. Jacobs, M. A. Mastro, B. N. Feigelson, A. Kuramata, P. Ye, S. Graham, B. B. Pate, K. D. Hobart, T. J. Anderson and M. J. Tadjer, *Appl. Phys. Lett.* 124, 153502 (2024).
30. N. K. Kalarickal, Z. Feng, A. Bhuiyan, Z. Xia, W. Moore, J. F. McGlone, A. R. Arehart, S. A. Ringel, H. Zhao and S. Rajan, *IEEE Transactions on Electron Devices* 68 (1), 29-35 (2020).
31. N. K. Kalarickal, Z. Xia, J. F. McGlone, Y. Liu, W. Moore, A. R. Arehart, S. A. Ringel and S. Rajan, *Journal of Applied Physics* 127 (21), 215706 (2020).
32. S. Saha, W. Amir, J. Liu, L. Meng, D. Yu, H. Zhao and U. Singiseti, *IEEE Electron Device Letters* 46(5), 725 (2025).
33. S. Sharma, L. Meng, A. Bhuiyan, Z. Feng, D. Eason, H. Zhao and U. Singiseti, *IEEE Electron Device Letters* 43 (12), 2029-2032 (2022).
34. C. N. Saha, A. Vaidya, A. Bhuiyan, L. Meng, S. Sharma, H. Zhao and U. Singiseti, *Appl. Phys. Lett.* 122, 182106 (2023).
35. H.-C. Huang, Z. Ren, A. Bhuiyan, Z. Feng, Z. Yang, X. Luo, A. Q. Huang, A. Green, K. Chabak, H. Zhao and X. Li, *Appl. Phys. Lett.* 121, 052102 (2022).
36. G. Alfieri, A. Mihaila, P. Godignon, J. B. Varley and L. Vines, *J. Appl. Phys.* 130, 025701 (2021).

37. J. Yang, Z. Sparks, F. Ren, S. J. Pearton and M. Tadjer, J. Vac. Sci. Technol. B 36, 061201 (2018).
38. Y. Zhang, A. Mauze and J. S. Speck, Appl. Phys. Lett. 115, 013501 (2019).
39. S. Rebollo, T. Itoh, S. Krishnamoorthy and J. S. Speck, Appl. Phys. Lett. 125, 012102 (2024).
40. H. Okumura and T. Tanaka, Japanese Journal of Applied Physics 58 (12), 120902 (2019).
41. M. Kim, H.-C. Huang, J. D. Kim, K. D. Chabak, A. R. K. Kalapala, W. Zhou and X. Li, Appl. Phys. Lett. 113, 222104 (2018).
42. H.-C. Huang, M. Kim, X. Zhan, K. Chabak, J. D. Kim, A. Kvit, D. Liu, Z. Ma, J.-M. Zuo and X. Li, ACS nano 13 (8), 8784-8792 (2019).
43. N. K. Kalarickal, A. Fiedler, S. Dhara, H.-L. Huang, A. Bhuiyan, M. W. Rahman, T. Kim, Z. Xia, Z. J. Eddine and A. Dheenan, Applied Physics Letters 119 (12), 123503 (2021).
44. S. Dhara, N. K. Kalarickal, A. Dheenan, S. I. Rahman, C. Joishi and S. Rajan, Appl. Phys. Lett. 123, 023503 (2023).
45. C. A. Gorsak, H. J. Bowman, K. R. Gann, J. T. Buontempo, K. T. Smith, P. Tripathi, J. Steele, D. Jena, D. G. Schlom, H. G. Xing, M. O. Thompson and H. P. Nair, Appl. Phys. Lett. 125, 242103 (2024).
46. T. Oshima and Y. Oshima, Appl. Phys. Lett. 124, 042110 (2024).
47. T. Oshima and Y. Oshima, Appl. Phys. Lett. 122, 162102 (2023).
48. T. Oshima and Y. Oshima, Applied Physics Express 16 (6), 066501 (2023).
49. S. A. Khan, A. Ibreljic and A. Bhuiyan, <https://doi.org/10.48550/arXiv.2506.17855> (Under Review) (2025).
50. S. Rafique, L. Han, A. T. Neal, S. Mou, J. Boeckl and H. Zhao, physica status solidi (a) 215 (2), 1700467 (2018).
51. X. Z. Liu, P. Guo, T. Sheng, L. X. Qian, W. L. Zhang and Y. R. Li, Optical Materials 51, 203-207 (2016).
52. Y. Chen, H. Liang, X. Xia, P. Tao, R. Shen, Y. Liu, Y. Feng, Y. Zheng, X. Li and G. Du, Journal of Materials Science: Materials in Electronics 26 (5), 3231-3235 (2015).
53. M. J. Tadjer, M. A. Mastro, N. A. Mahadik, M. Currie, V. D. Wheeler, J. A. Freitas Jr, J. D. Greenlee, J. K. Hite, K. D. Hobart and C. R. Eddy Jr, Journal of Electronic Materials 45 (4), 2031-2037 (2016).
54. P. Ma, J. Zheng, X. Liu, Z. Liu, Y. Zuo and B. Cheng, Journal of Semiconductors 45 (2), 022502 (2024).
55. C. Kranert, C. Sturm, R. Schmidt-Grund and M. Grundmann, Sci Rep 6, 35964 (2016).
56. H. Okumura, Y. Kato, T. Oshima and T. Palacios, Japanese Journal of Applied Physics 58 (SB), SBBD12 (2019).
57. R. Lingaparthi, K. Sasaki, Q. T. Thieu, A. Takatsuka, F. Otsuka, S. Yamakoshi and A. Kuramata, Applied Physics Express 12 (7), 074008 (2019).
58. X. Lu, X. Zhou, H. Jiang, K. W. Ng, Z. Chen, Y. Pei, K. M. Lau and G. Wang, IEEE Electron Device Letters 41 (3), 449-452 (2020).

59. S. Saha, L. Meng, Z. Feng, A. Bhuiyan, H. Zhao and U. Singiseti, *Applied Physics Letters* 120 (12), 122106 (2022).
60. C. J. Klingshirn, A. Jayawardena, S. Dhar, R. P. Ramamurthy, D. Morissette, T. Zheleva, A. Lelis and L. G. Salamanca-Riba, *J. Appl. Phys.* 129, 195705 (2021).
61. Z. Jian, S. Mohanty and E. Ahmadi, *Appl. Phys. Lett.* 116, 152104 (2020).
62. A. Jayawardena, A. C. Ahyi and S. Dhar, *Semiconductor Science and Technology* 31 (11), 115002 (2016).
63. K. Ghosh and U. Singiseti, *Applied Physics Letters* 109 (7), 072102 (2016).
64. L. Zhou, H. Chen, T. Xu, J. Ruan, Y. Lai, Y. Deng, J. Chen, X. Zou, X. Lu, L. Chen and X. Ouyang, *Appl. Phys. Lett.* 124, 013506 (2024).
65. J. H. Werner and H. H. Güttler, *Journal of Applied Physics* 69 (3), 1522-1533 (1991).
66. R. T. Tung, *Appl. Phys. Rev.* 1, 011304 (2014).
67. R. T. Tung, *Physical Review B* 45 (23), 13509-13523 (1992).
68. W. Mönch, *Applied Physics A* 87 (3), 359-366 (2007).
69. W. Mönch, *Journal of Vacuum Science & Technology B: Microelectronics and Nanometer Structures Processing, Measurement, and Phenomena* 17 (4), 1867-1876 (1999).
70. P. R. S. Reddy, V. Janardhanam, K.-H. Shim, V. R. Reddy, S.-N. Lee, S.-J. Park and C.-J. Choi, *Vacuum* 171, 109012 (2020).
71. H. Sheoran, B. R. Tak, N. Manikanthababu and R. Singh, *ECS Journal of Solid State Science and Technology* 9 (5), 055004 (2020).
72. C. Fares, F. Ren and S. J. Pearton, *ECS Journal of Solid State Science and Technology* 8 (7), Q3007 (2019).

Figure 1

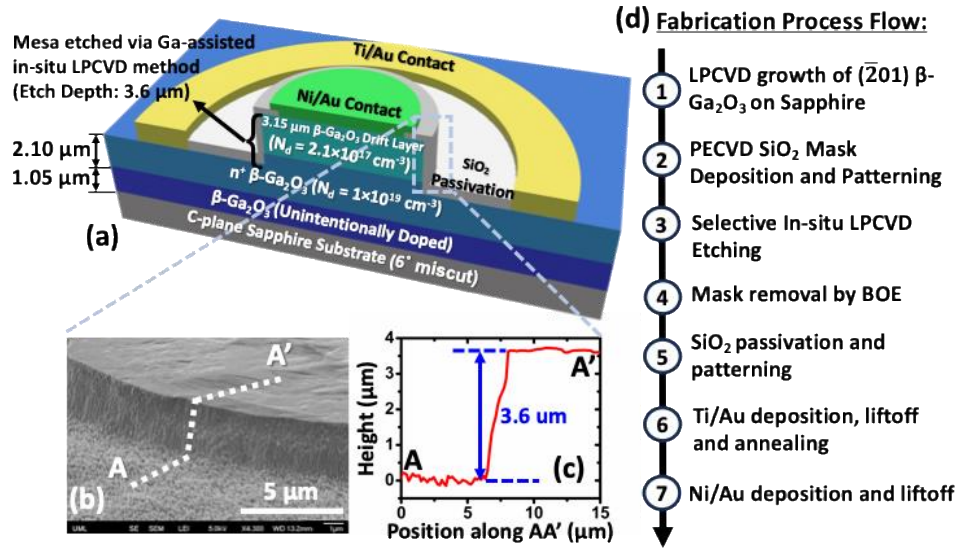


Figure 1. (a) Schematic cross-section of the quasi-vertical Schottky barrier diode (SBD) fabricated using LPCVD grown (201) β -Ga₂O₃ film on a 6° miscut c-plane sapphire substrate. The device features a three-layer epitaxial stack: a 1.05 μm unintentionally doped (UID) buffer layer, a 2.10 μm thick n^+ β -Ga₂O₃ contact layer ($N_d = 1 \times 10^{19} \text{ cm}^{-3}$), and a 3.15 μm β -Ga₂O₃ drift layer ($N_d = 2.1 \times 10^{17} \text{ cm}^{-3}$). Plasma-free LPCVD etching was used to etch 3.6 μm into the β -Ga₂O₃ drift layer for mesa isolation and to expose the n^+ layer for anode contact formation. (b) Tilted (60° tilt) Cross-sectional FESEM image showing the etch sidewall profile with an etch depth of 3.6 μm . (c) AFM line scan along the AA' cutline over etched mesa region confirming the etch depth of 3.6 μm . (d) Step by-step fabrication process flow including LPCVD growth, in-situ etching, and metallization steps for device realization.

Figure 2

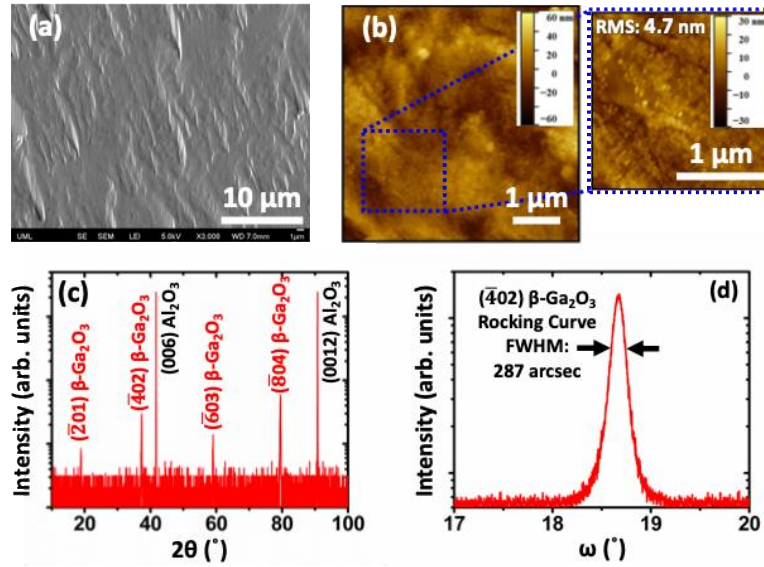


Figure 2. Structural and surface morphological characterization of the LPCVD-grown heteroepitaxial $(\bar{2}01)$ β -Ga₂O₃ epitaxial stack used in device fabrication. (a) Top-view FESEM image showing clear step-flow surface morphology, indicative of high crystalline quality and epitaxial layer-by-layer growth. (b) AFM scan of the film surface reveals smooth morphology with a root mean square (RMS) roughness of 4.7 nm. (c) XRD ω -2 θ scan showing strong diffraction peaks corresponding to the $(\bar{h}0l)$ family of $(\bar{2}01)$ β -Ga₂O₃, along with sapphire substrate peaks, confirming phase purity and preferred orientation. (d) XRD ω -rocking curve of the $(\bar{4}02)$ reflection exhibiting a narrow full width at half maximum (FWHM) of 287 arcsec, indicating the high crystalline quality of the β -Ga₂O₃ epitaxial stack.

Figure 3

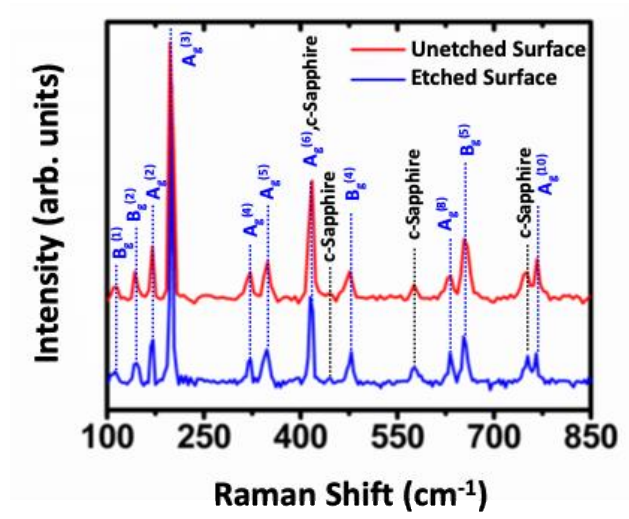


Figure 3. Room temperature Raman spectra of the LPCVD-grown heteroepitaxial ($\bar{2}01$) β -Ga₂O₃ surface before (red) and after (blue) Ga-assisted in-situ LPCVD etching. Both spectra exhibit sharp and well-defined A_g and B_g phonon modes characteristic of monoclinic β -Ga₂O₃, confirming structural integrity and phase purity. Peaks from the c-plane sapphire substrate are also visible in both spectra.

Figure 4

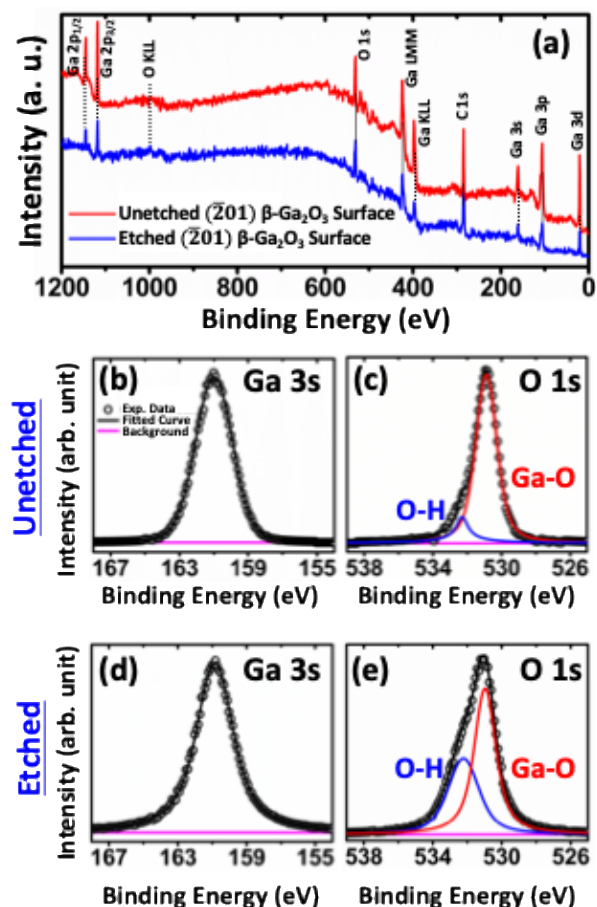


Figure 4. X-ray photoelectron spectroscopy (XPS) analysis of LPCVD-grown β -Ga₂O₃ surfaces before and after Ga-assisted in-situ etching. (a) Wide-scan XPS survey spectra showing Ga and O signals, with no detectable contamination from extrinsic elements. (b, c) High-resolution Ga 3s and O 1s spectra of the unetched surface. (d, e) Corresponding spectra for the etched surface. The O 1s peaks are deconvoluted into lattice oxygen (Ga-O) and surface hydroxyl (O-H) components. The spectra confirm chemical purity and near-stoichiometric composition for both surfaces, with no significant changes in bonding states after etching, indicating that the LPCVD etch process preserves surface chemistry and structural integrity.

Figure 5

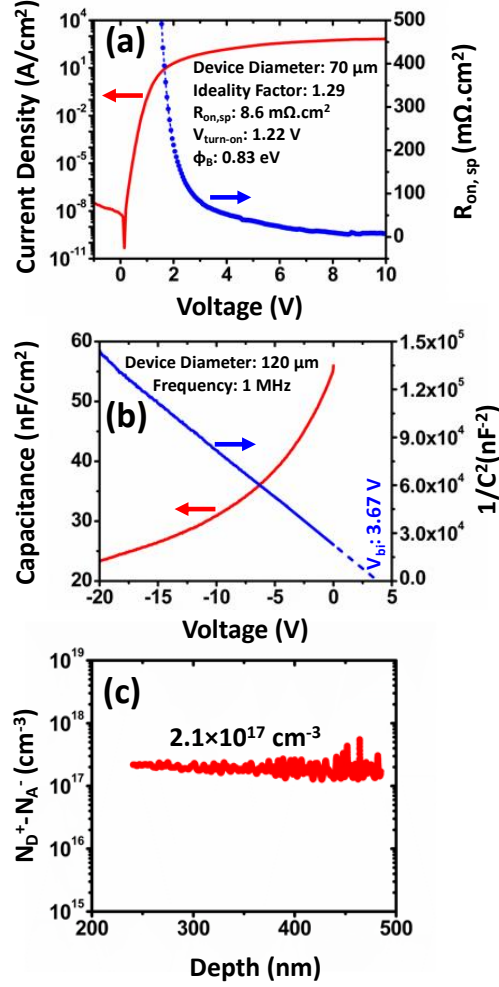


Figure 5. (a) Forward I-V characteristics and extracted specific on-resistance ($R_{on,sp}$) of the quasi-vertical $\beta\text{-Ga}_2\text{O}_3$ Schottky diode with a 70 μm diameter. The device exhibits an ideality factor of 1.29, a turn-on voltage ($V_{\text{turn-on}}$) of 1.22 V, a Schottky barrier height (Φ_B) of 0.83 eV, and a minimum differential $R_{on,sp}$ of 8.6 $\text{m}\Omega \cdot \text{cm}^2$. (b) C-V and $1/C^2$ -V characteristics measured at 1 MHz for a 120 μm diameter device. (c) Net carrier density profile ($N_D^+ - N_A^-$) showing uniform doping of $\sim 2.1 \times 10^{17} \text{ cm}^{-3}$ in the $\beta\text{-Ga}_2\text{O}_3$ drift layer, extracted from the C-V curve.

Figure 6

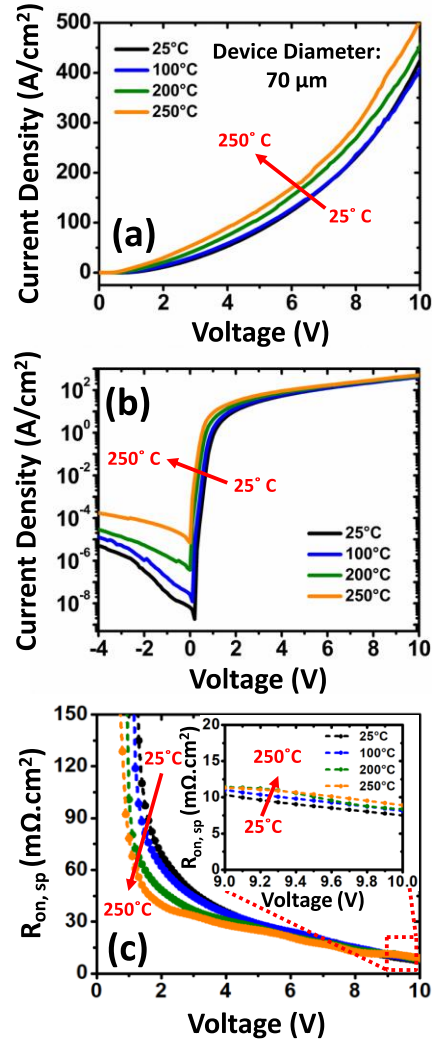


Figure 6. Temperature-dependent current-voltage (J-V-T) characteristics of a 70 μm diameter quasi-vertical $\beta\text{-Ga}_2\text{O}_3$ SBD measured at 25°C, 100°C, 200°C, and 250°C. (a) Forward J–V characteristics showing a monotonic increase in on-current density with temperature. (b) Semi-log J-V plot showing higher leakage current at elevated temperatures. (c) Extracted specific on-resistance ($R_{\text{on,sp}}$) versus forward bias voltage at different temperature.

Figure 7

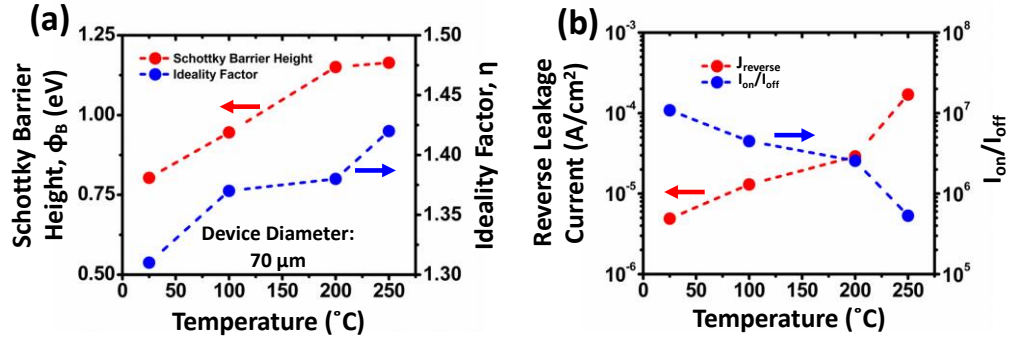


Figure 7. Temperature-dependent Schottky diode performance metrics. (a) Extracted Schottky barrier height (Φ_B) and ideality factor (η) as a function of temperature, showing an increase in Φ_B and η with rising temperature. (b) Reverse leakage current (J_{reverse}) and on/off current ratio ($I_{\text{on}}/I_{\text{off}}$) versus temperature, illustrating the thermally activated increase in leakage and corresponding reduction in rectification ratio at elevated temperatures.

Figure 8

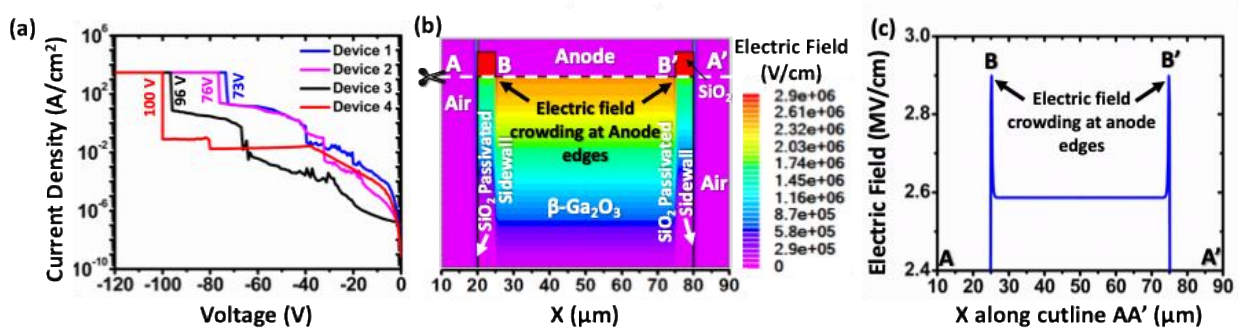


Figure 8. (a) Reverse J-V characteristics of four quasi-vertical β -Ga₂O₃ SBDs, showing breakdown voltages ranging from 73 V to 100 V, corresponding to parallel-plate electric field strengths between 1.66 MV/cm and 1.94 MV/cm. (b) TCAD-simulated 2D electric field distribution under reverse bias conditions (at 100V), revealing strong electric field crowding near the anode perimeter. (c) 1D electric field profile extracted along the cutline AA', further confirming peak field intensification at the anode edges.